Polarization effects in quantum coherences probed by two-color, resonant four-wave mixing in the time domain

E. F. McCormack and E. Sarajlic
Physics Department, Bryn Mawr College, Bryn Mawr, Pennsylvania 19010
(Received 20 June 2000; published 16 January 2001)

We present a combined theoretical and experimental study of the effects of laser polarization on optical coherences produced in two-color, resonant four-wave mixing (TC-RFWM). A time-dependent model incorporating diagrammatic perturbation theory and spherical tensor formalism is used to interpret observations of quantum beats due to molecular hyperfine structure in time-resolved TC-RFWM in nitric oxide. Good agreement is found between the model and the observed time-resolved signals for two distinct excitation schemes and a variety of polarization configurations including both polarization and population gratings. Measured hyperfine energy intervals are reported for the $X\,^2\Pi_{1/2}$, $v=0$ ground state and the $A\,^2\Sigma^+$, $v=0$ excited state of NO. The experimental results demonstrate that TC-RFWM can be used to perform state-selective, quantum beat spectroscopy in three-level systems by suitably designing three experimental features: the excitation scheme for the matter-field interaction, the time ordering of the laser pulses, and the polarization of the incident laser beams.

DOI: 10.1103/PhysRevA.63.023406 PACS number(s): 42.50.Md, 42.65.Hw, 33.40.+f, 33.20.−t

I. INTRODUCTION

Resonant four-wave mixing (RFWM) is a nonlinear optical technique that provides a versatile spectroscopic and diagnostic tool for probing stable and transient atomic and molecular species in a variety of condensed and gas-phase environments. It is based on a nonlinear optical process in which three coherent light beams interact with a medium via the third-order nonlinear susceptibility, $\chi^{(3)}$, to create a fourth, new, coherent light beam [1]. The efficiency of the process is greatly enhanced when the frequencies of the interacting light beams are resonant with a set of optical transitions in the medium, which gives the technique a natural application in spectroscopy. In frequency-resolved applications, spectra are obtained by scanning the frequency of any one of the input laser fields over selected resonances. In the time domain, the RFWM signal is detected as a function of the time delays between the input laser pulses. A number of reviews highlight many of the successful applications of this type of nonlinear optical probe in both the frequency and time domains to study atomic and molecular structure and dynamics [2–7].

Both frequency- and time-domain RFWM benefit from the coherent, background free, and highly directional nature of the light produced, which makes these techniques particularly amenable to noninvasive, remote sensing applications. In particular, since the signal generation in RFWM is entirely absorption based, this technique can be used effectively in gas-phase studies of the molecular structure and dynamics of excited states that do not readily decay via photon emission or do not have favorable ionization cross sections. Useful RFWM techniques used to study gas-phase samples in the time domain include, time-resolved degenerate four-wave mixing (DFWM), time-resolved coherent anti-Stokes Raman scattering (CARS), and photon echo spectroscopy [8,9]. By using intense, ultrafast laser pulses, time-resolved RFWM can attain high sensitivity and excellent temporal resolution, providing a valid alternative to other time-domain techniques such as laser-induced fluorescence, resonant impulsive stimulated Raman scattering, Rayleigh scattering, stimulated emission pumping, and multiphoton ionization [10]. Indeed, picosecond and femtosecond DFWM and CARS have been successfully applied to the probing of electronic and rovibrational dynamics in molecules [11–14] real-time studies of gas-phase reactions [15], and measurements of macroscopic observables, such as temperature and pressure gradients, in flames [16–18].

In the special case of two-color, resonant four-wave mixing, (TC-RFWM), where the incident light frequencies are resonant with two distinct transitions in the medium, specific advantages are inherent [19]. The first is that by using two different transition frequencies, a variety of excitation schemes are allowed. This flexibility in implementation has been exploited in frequency-domain experiments to perform, for example, nonlinear stimulated emission pumping spectroscopy [20,21], to detect highly predissociative molecular states [22,23], and to study saturation effects in photolysis processes [24]. The second is the state selectivity offered by the double-resonance condition in TC-RFWM processes, which can facilitate the analysis of rovibrational molecular spectra [25] and the detection of multistate interaction effects [26].

Of particular interest to the results presented here are recent theoretical investigations of TC-RFWM in the time domain where the coherent excitation of material superposition states leads to quantum interference in the four-wave mixing process that manifests as quantum beats in the detected signal [27]. This paper suggests that TC-RFWM should allow for a markedly different type of state selectivity based on the control of the resonant contributions to the third-order susceptibility through the choice of laser polarization, laser pulse time ordering, and excitation scheme. It is this potential for control that makes using TC-RFWM to explore molecular structure and dynamics so attractive. The physical type of coherently excited levels that can be probed is deter-

mined by the particular time characteristics of the TC-RFWM experiment under consideration. For example, microsecond and nanosecond laser pulses can be used to prepare hyperfine, Zeeman, and Stark coherences in atoms and molecules with nonzero nuclear spin [28–32]. Picosecond and femtosecond pulses can be used to create rotational wave packets [33] and vibrational superposition states [13,34] within molecular electronic states or coherently excited fine-structure energy levels in atoms [15].

TC-RFWM quantum beats were first observed in gas-phase samples by Rose and coworkers [35] who detected ground-state hyperfine quantum beats in sodium vapor. McCormack *et al.* [29] observed quantum beats due to the hyperfine structure of an excited electronic state in nitric oxide and Motzkus, Pedersen, and Zewail [15] reported the detection of quantum beats corresponding to the fine-structure splitting of the $3p$ state in sodium. These studies clearly show the potential of TC-RFWM for performing high-resolution spectroscopy of unresolved energy states within electronic or rovibronic manifolds and highlight the important issue of laser polarization in the selective observation of the quantum interferences of the field-matter interactions. Here we present observations of quantum beats due to molecular hyperfine structure in time-resolved TC-RFWM in nitric oxide (NO) using two excitation schemes employing several different polarizations configurations. The new results are compared to the predictions of a theoretical model for TC-RFWM [27], which uses a general theoretical treatment combining diagrammatic perturbation theory and the spherical tensor formalism [36–38] and is expressed in the Liouville-space mathematical framework [9]. The experimental results demonstrate that TC-RFWM can be used to perform, high-resolution, state-selective quantum beat spectroscopy, where the type of quantum interference observed can be controlled by suitably designing the excitation scheme for the matter-field interaction, the time-ordering of the laser pulses, and the polarization of the incident laser beams. The results also highlight the potential for using TC-RFWM techniques in the coherent control of field-matter interactions.

The remainder of the paper is organized into five sections. In Sec. II we begin with some background on our implementation of TC-RFWM and the hyperfine structure of the $X\,^2\Pi_{1/2}$, $v=0$ ground state and $A\,^2\Sigma^+$, $v=0$ excited state of NO. In Sec. III we present, for a given choice of excitation scheme and experimental geometry, theoretical expressions for time-dependent TC-RFWM signal intensities as a function of laser-pulse polarization. In Sec. IV we describe the experimental arrangement, conditions, and procedures for acquiring time-dependent TC-RFWM signals. In Sec. V we present measurements of the time behavior of the RFWM signals for several different rovibrational transitions in the NO molecule as a function of polarization configurations and excitation scheme. Measured hyperfine energy intervals for the $X\,^2\Pi_{1/2}$, $v=0$ state and the $A\,^2\Sigma^+$, $v=0$ state are reported. There we also compare the experimental results to the predictions of the model and discuss the successes and limitations of the model. In Sec. VI we present the conclusions of our findings.

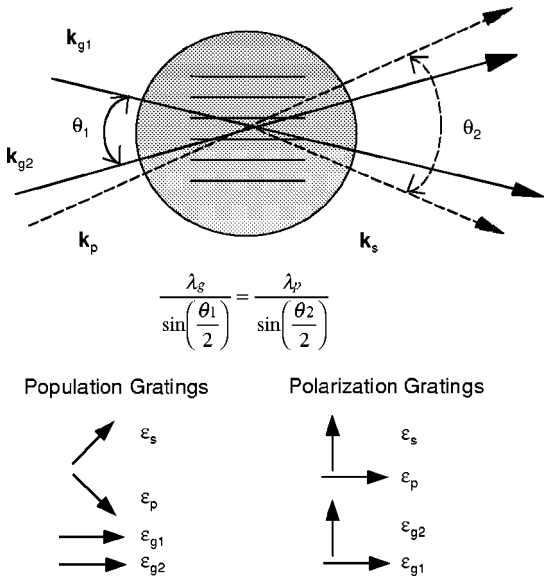

FIG. 1. TC-RFWM as a process of creating and probing laser-induced gratings.

II. BACKGROUND

A. TC-RFWM as laser-induced gratings

The consideration of TC-RFWM signal generation in terms of the scattering of light from laser-induced gratings has provided a useful conceptual basis for our understanding of these processes and is the basis of the notation we will use [39]. In this picture, depicted schematically in Fig. 1, two laser beams, denoted by the wave vectors $\mathbf{k}_{g1}$ and $\mathbf{k}_{g2}$, overlap at a small angle in the absorbing medium and produce a spatial variation of total light intensity or total field polarization. This variation constitutes a spatial modulation of the complex refractive index of the medium, which acts as a three-dimensional diffraction grating that scatters the probe beam $\mathbf{k}_p$ and produces the coherent signal beam $\mathbf{k}_s$. The phase-matching requirements for the mixing is equivalent to the Bragg scattering condition. This conceptual picture is particularly apt for describing the particular time-ordering considered here where the two grating laser pulses arrive simultaneously, followed by a delayed third laser pulse (the probe) which simultaneously produces the signal laser pulse. In this picture, the time evolution of the grating is sampled by the probe providing information about the intermolecular dynamics of the sample, as well as the dynamics of the matter states involved in the grating production. The grating configuration where the two grating-forming beams have parallel linear polarizations is referred to as a population grating and the configuration where the two grating beams have orthogonal polarizations is called a polarization grating.

We consider two excitation schemes denoted Ξ and V and shown in Fig. 2. Rotational transitions between the electronic ground state and excited states of NO allow us to study the polarization dependencies of the TC-RFWM processes as a function of probe pulse delay for these two different excitation schemes. In addition to the expected decay of the laser-induced grating signal due to molecular lifetimes and molecular motion, the time dependence of the signal beam can

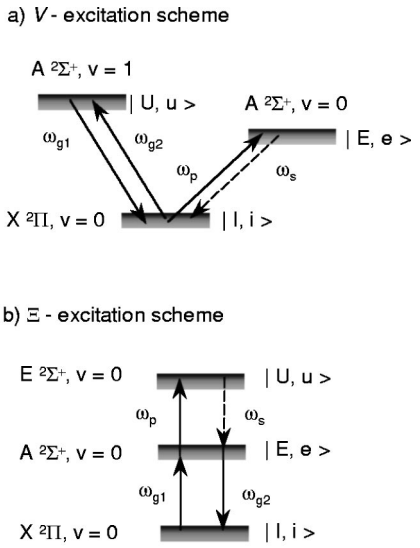

FIG. 2. Excitation schemes for TC-RFWM. (a) V scheme and (b) Ξ scheme.

exhibit strong interference effects due to the coherent excitation of spectrally unresolved states. The unresolved states that lead to these quantum beats in the time evolution of the induced gratings investigated here, are due to the hyperfine structure of the molecular states reflecting the interaction of nuclear and electronic spin and rotation in the molecule.

B. Spectroscopic considerations

Figure 3 depicts the hyperfine structure of the $N=2$ levels of the $X\,^2\Pi_{1/2}$, $v=0$ ground state and the $A\,^2\Sigma^+$, $v=0$ excited state of NO. The $X\,^2\Pi$, $v=0$ state is split by the spin-orbit interaction into a $^2\Pi_{1/2}$ and $^2\Pi_{3/2}$ component separated by about 123 cm^{-1}. We consider here the $^2\Pi_{1/2}$ component since all the data presented involve only this level. The electronic angular momentum **J** is the sum of the total angular momentum exclusive of electronic spin **N**, and the electronic spin **S**. For the $^2\Pi_{1/2}$ component, $\mathbf{J}=\mathbf{N}+1/2$. The Λ-doubling interaction splits the $^2\Pi_{1/2}$ component into positive, $e(+)$, and negative, $f(-)$, levels. The nuclear spin **I**, then couples with **J**, to form **F**, the total angular momentum of the system. With $\mathbf{I}=1$ for NO, each member of the Λ doublet is split by hyperfine interactions into three levels. The hyperfine structure of the ground state has been measured by numerous authors and the results have been gathered by Kirstiansen to generate accurate hyperfine parameters [40]. The results given there are in the form of hyperfine energy intervals and we can make a direct comparison with our data.

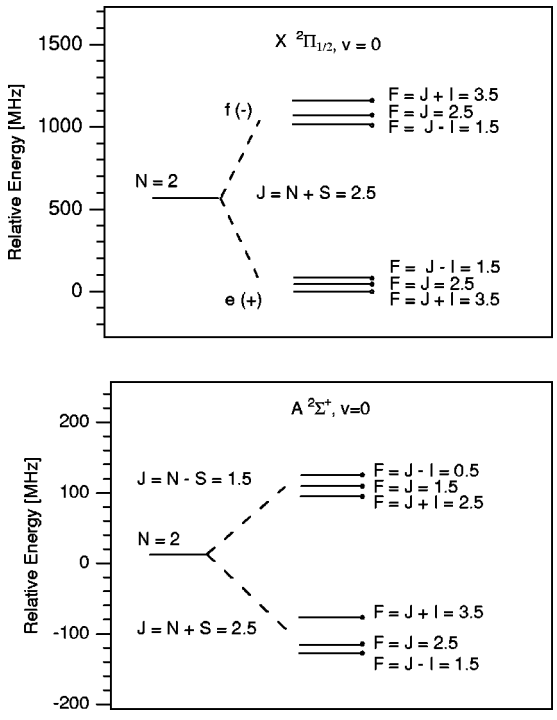

FIG. 3. Hyperfine structure of the $N=2$ levels of the $X\,^2\Pi_{1/2}$, $v=0$ ground state and $A\,^2\Sigma^+$, $v=0$ excited state of NO.

The excited $A\,^2\Sigma^+$, $v=0$ state is a low-lying Rydberg state and, as in the ground state, the total angular momentum exclusive of spin **N**, couples to **S**, the electronic spin, to give the angular momentum $\mathbf{J}=\mathbf{N}+\mathbf{S}$. Fine-structure interactions cause these levels to split into levels with $\mathbf{J}=\mathbf{N}\pm 1/2$. The nuclear spin **I**, then couples with **J**, to form **F**, the total angular momentum of the system. Hyperfine structure parameters have been determined for the $A\,^2\Sigma^+$, $v=1$, and $v=3$ states using a range of spectroscopic techniques, including optical radio-frequency double resonance [41], and more recently, ultrahigh resolution two-photon spectroscopy [42]. To make a comparison of our data to those previous results we used the constants derived from these studies to compute the hyperfine energy intervals in the $A\,^2\Sigma^+$, $v=1$, and $v=3$ vibrational states following the approach outlined by Bergeman and Zare [41].

Rotational transitions between the $X\,^2\Pi_{1/2}$, $A\,^2\Sigma^+$, and $E\,^2\Sigma^+$ states used in the excitation schemes shown in Fig. 2 are denoted in the standard manner by using the $P(J)$, $Q(J)$, and $R(J)$ branch notation, where J is the lower J value in the transition. P denotes $\Delta J=-1$, Q denotes $\Delta J=0$, and R denotes $\Delta J=+1$.

III. THEORETICAL EXPRESSIONS

A. TC-RFWM model

Here we follow the development in Ref. [27] to present theoretical expressions for the time-dependent TC-RFWM signal produced in the Ξ- and V-excitation schemes shown in Fig. 2. The model uses diagrammatic perturbation theory and a spherical tensor formalism to compute the signal intensity and it includes a treatment of interference effects due to coherent excitation of spectrally unresolved states. It considers a three-level system in which the states are connected by one-photon transitions and separated by energies that are well outside the laser bandwidth. The model requires that the states of the system have a well-defined total angular momentum and that the initial state of the system be characterized by a uniform and incoherent population in the magnetic sublevels.

In the weak-field regime the signal intensity of a four-wave mixing process is proportional to the time average of the third-order dielectric polarization induced by the electric fields of the interacting laser beams:

$$\mathcal{J} \propto \langle |\mathbf{P}^{(3)}(\mathbf{r},t)|^2 \rangle. \tag{1}$$

Assuming only the lowest rank matter-field multipole interaction, the polarization is given by the expectation value of the single-particle electric dipole operator,

$$\mathbf{P}^{(3)}(\mathbf{r},t) = \langle\langle \mu | \rho^{(3)}(\mathbf{r},t) \rangle\rangle, \tag{2}$$

where $|\mu\rangle\rangle$ and $|\rho^{(3)}(\mathbf{r},t)\rangle\rangle$ denote Liouville-space state vectors corresponding to the electric dipole moment and third-order component of the density operator, $|\rho(\mathbf{r},t)\rangle\rangle$, respectively [9].

The model assumes that the incident fields are infinitely short, ideal broadband pulses given by

$$\mathbf{E}_i(\mathbf{r},t) = \mathcal{E}_i \varepsilon_i \delta(t-\tau_i) \exp(-i\omega_i \tau_i + i\mathbf{k}_i \cdot \mathbf{r}) + \text{c.c.}, \tag{3}$$

where ω_i, $\mathcal{E}_i$, ε_i, τ_i, and $\mathbf{k}_i$ are the central frequency, complex amplitude, the complex polarization unit vector, the arrival time, and the wave vector of an incident beam *i*, respectively. The index *i* refers to the probe beam or one of the two grating beams. The interactions of these fields with the medium matter density operator can be represented in the form of double sided Feynman diagrams that depict the resonant sequences of the photon-matter interactions for a given excitation scheme [27,43]. For the Ξ-excitation scheme shown in Fig. 2(b), and simultaneous grating pulses and a probe pulse delayed by τ, this procedure yields the following expression for the third-order component of the density operator:

$$\begin{aligned} |\rho^{(3)}(\mathbf{r},t)\rangle\rangle = \frac{N}{i\hbar^3} \mathcal{E}_p \mathcal{E}^*_{g_2} \mathcal{E}_{g_1} \exp(-i\omega_p t + i\mathbf{k}_s \cdot \mathbf{r}) \\ \times \sum_{i,e,e',u} \sum_{\text{all } M} \langle u|\varepsilon_p \cdot \mu|e\rangle\langle e|\varepsilon_{g_1} \cdot \mu|i\rangle \\ \times \langle i|\varepsilon^*_{g_2} \cdot \mu|e'\rangle \exp(-i\Omega_{ee'}\tau)|ue'\rangle\rangle), \end{aligned} \tag{4}$$

where $|\alpha\rangle$, $\alpha = ``i,'' ``e,''$ and ``*u*,'' specifies hyperfine levels of the states $|I\rangle$, $|E\rangle$, and $|U\rangle$, respectively. The complex frequency $\Omega_{ee'}$ associated with the evolution of the state vector $|ee'\rangle\rangle$, is given by

$$\Omega_{ee'} = \omega_{ee'} - i\Gamma_{ee'}. \tag{5}$$

Here, $\hbar\omega_{ee'}$ represents the energy difference between the states $|e\rangle$ and $|e'\rangle$, and $\Gamma_{ee'}$ is the sum of the average decay rate of those states and the rate of dephasing of the $|e\rangle\langle e'|$ coherence. By substituting Eq. (4) into Eqs. (1) and (2), the expression for the signal intensity as a function of the time delay between the grating and the probe pulses τ, becomes

$$\begin{aligned} \mathcal{J}(\tau) \propto \Bigg| \sum_{i,e,e',u} \sum_{\text{all } M} \langle e'|\varepsilon^*_s \cdot \mu|u\rangle\langle u|\varepsilon_p \cdot \mu|e\rangle\langle e|\varepsilon_{g_1} \cdot \mu|i\rangle \\ \times \langle i|\varepsilon^*_{g_2} \cdot \mu|e'\rangle \exp(-i\Omega_{ee'}\tau) \Bigg|^2, \end{aligned} \tag{6}$$

where ε_s is the complex polarization unit vector of the signal beam.

The evaluation of the four photon matrix element product is made by the use of a spherical tensor formalism. Expressing the polarization vectors and dipole moment operators in a spherical basis enables us to apply the Wigner-Eckart theorem and rewrite the matrix elements in terms of their corresponding reduced matrix elements and vector coupling coefficients [44]. After performing these algebraic steps specified in Ref. [27], we arrive at the following expression for signal intensity

$$\begin{aligned} \mathcal{J}(\tau) \propto |\langle J_E \| \mu^{[1]} \| J_I \rangle|^4 |\langle J_U \| \mu^{[1]} \| J_E \rangle|^4 \\ \times \Bigg| \sum_{e,e'} \mathfrak{F}_\Xi(F_e, F_{e'}; \varepsilon^*_s, \varepsilon_p, \varepsilon_{g_1}, \varepsilon^*_{g_2}) \\ \times \exp(-i\Omega_{ee'}\tau) \Bigg|^2, \end{aligned} \tag{7}$$

where $|\langle J_U \| \mu^{[1]} \| J_I \rangle|^2$ and $|\langle J_E \| \mu^{[1]} \| J_I \rangle|^2$ are reduced matrix elements proportional to the Einstein coefficients for the transitions $|I\rangle \leftrightarrow |U\rangle$ and $|I\rangle \leftrightarrow |E\rangle$, respectively. The reduced matrix elements depend on the molecular wave function in the frame of the molecule, and are therefore independent of the molecular orientation [44]. The $\mathfrak{J}_\Xi$ factor contains all the geometric information about the coupling of angular momenta of photons in specific polarization states to the total angular momentum of the hyperfine states:

$$\begin{aligned} \mathfrak{F}_\Xi(F_{e'}, F_e; \varepsilon^*_s, \varepsilon_p, \varepsilon_{g_1}, \varepsilon^*_{g_2}) \\ = (2F_{e'}+1)(2F_e+1)(-1)^{F_{e'}+F_e} \\ \times (-1)^{J_U+J_E} \sum_{i,\mu} \sum_{q_1,q_2,q_3=-1}^{1} \sum_{x=0}^{2} (-1)^{x+q_2+q_3+2F_i} \\ \times (2x+1)(2F_i+1)(2F_u+1)(\varepsilon^*_s)^{[1]}_{q_1}(\varepsilon_p)^{[1]}_{q_2}(\varepsilon_{q_1})^{[1]}_{q_3} \\ \times (\varepsilon^*_{g_2})^{[1]}_{-q_1-q_2-q_3} \begin{pmatrix} 1 & x & 1 \\ q_1 & q_2+q_3 & -q_1-q_2-q_3 \end{pmatrix} \\ \times \begin{pmatrix} 1 & x & 1 \\ q_2 & -q_2-q_3 & q_3 \end{pmatrix} \begin{Bmatrix} 1 & x & 1 \\ F_i & F_{e'} & F_u \end{Bmatrix} \\ \times \begin{Bmatrix} 1 & x & 1 \\ F_i & F_e & F_u \end{Bmatrix} \begin{Bmatrix} F_{e'} & F_u & 1 \\ J_U & J_E & \mathcal{I} \end{Bmatrix} \begin{Bmatrix} F_u & F_e & 1 \\ J_E & J_U & \mathcal{I} \end{Bmatrix} \\ \times \begin{Bmatrix} F_e & F_i & 1 \\ J_I & J_E & \mathcal{I} \end{Bmatrix} \begin{Bmatrix} F_i & F_{e'} & 1 \\ J_E & J_I & \mathcal{I} \end{Bmatrix}. \end{aligned} \tag{8}$$

Here the () and {} arrays denote the 3-*j* and 6-*j* vector coupling coefficients, respectively [45]. We see that for the Ξ-excitation scheme, the behavior of the RFWM signal as a function of the delay of the probe pulse τ, is given by the energy separations between the hyperfine levels of the intermediate $A\,^2\Sigma^+$, $v=0$ state.

For the *V*-excitation scheme shown in Fig. 2(a), an analogous procedure yields

$$\mathcal{I}(\tau)\propto|\langle J_U\|\mu^{[1]}\|J_I\rangle|^4|\langle J_E\|\mu^{[1]}\|J_I\rangle|^4 \times\left|\sum_{i,i'}\mathfrak{F}_V(F_i,F_{i'};\varepsilon_s^*,\varepsilon_p,\varepsilon_{g_2}^*,\varepsilon_{g_1}\exp(-i\Omega_{i'i}\tau)\right|^2. \tag{9}$$

In this case, $\mathfrak{F}_V$ is given by

$$\begin{aligned}\mathfrak{F}_V(F_i,F_{i'};\varepsilon_s^*,\varepsilon_p,\varepsilon_{g_2}^*,\varepsilon_{g_1})&=(2F_i+1)(2F_{i'}+1)(-1)^{F_i+F_{i'}}\\&\times(-1)^{J_U+J_E}\sum_{e,u}\sum_{q_1,q_2,q_3=-1}^{1}\sum_{x=0}^{2}(-1)^{x+q_2+q_3+2F_e}\\&\times(2x+1)(2F_i+1)(2F_u+1)(\varepsilon_s^*)_{q_1}^{[1]}(\varepsilon_p)_{q_2}^{[1]}(\varepsilon_{g_2}^*)_{q_3}^{[1]}\\&\times(\varepsilon_{g_1})_{-q_1-q_2-q_3}^{[1]}\begin{pmatrix}1&x&1\\q_1&q_2+q_3&-q_1-q_2-q_3\end{pmatrix}\\&\times\begin{pmatrix}1&x&1\\q_2&-q_2-q_3&q_3\end{pmatrix}\begin{Bmatrix}1&x&1\\F_e&F_i&F_u\end{Bmatrix}\\&\times\begin{Bmatrix}1&x&1\\F_e&F_{i'}&F_u\end{Bmatrix}\begin{Bmatrix}F_i&F_u&1\\J_U&J_I&\mathcal{I}\end{Bmatrix}\begin{Bmatrix}F_u&F_{i'}&1\\J_I&J_U&\mathcal{I}\end{Bmatrix}\\&\times\begin{Bmatrix}F_{i'}&F_e&1\\J_E&J_I&\mathcal{I}\end{Bmatrix}\begin{Bmatrix}F_e&F_i&1\\J_I&J_E&\mathcal{I}\end{Bmatrix}.\end{aligned} \tag{10}$$

Here we see that for the *V*-excitation scheme, the beats correspond to energy separations between the hyperfine levels in the $X\,^2\Pi_{1/2}$, $v=0$ ground state.

B. Angular momentum distributions

Many recent developments in applying RFWM techniques have focused explicitly on exploiting the dependence of RFWM signals on laser polarization to probe the different dynamics of the angular momentum population, orientation, and alignment contributions in a given sample [6,11,14,27,36,46–50]. How this can be achieved is expressed in Eqs. (8) and (10). They give a description of coherences induced by the laser field-matter interactions in terms of the total angular momentum distributions expressed as a sum of state multipoles, which transform as irreducible tensors of rank *x* and component *q* [39,44]. The physical interpretation of these tensors is the following: the rank 0 tensor represents the population, the rank 1 the orientation, and the rank 2 the alignment of the total angular momentum state of the system [44,47]. In the diagrammatic perturbative treatments, such as the one described here, the induced third-order susceptibility is proportional to the product of four-photon matrix elements that couple pairs of unresolved hyperfine levels in distinct electronic states. Permutations of these matrix elements describe different time orderings of the field-matter interactions, i.e., photon production or annihilation events. In the general case of temporally overlapped beams, there are many terms that can contribute to the signal intensity. In the treatment by Williams *et al.* [18], the summation over different four-photon matrix elements is simplified by rearranging the matrix elements, which does not affect the final signal intensity. However, as they point out, this permutation changes the order of the angular momentum coupling in their treatment and takes away the physical significance of the $x=0,1,2$ terms as being pure contributions from the rank 0, 1, 2 state multipoles of the system.

In the fully resonant process considered here with simultaneous grating pulses and a delayed probe pulse, however, there are only two time orderings that give significant contributions to the resonant generation of the signal [27] and thus, there is no reordering of the matrix elements in the summation in Eqs. (8) and (10), thereby preserving the physical meaning of the coupling rank *x*. If we think in terms of laser-induced gratings, one can extract the contributions of the population, orientation, and alignment gratings to the total diffracting grating by judiciously choosing polarization configurations for a given set of rotational transitions. This can be very useful in the interpretation of studies of relaxation and dephasing rates for induced populations and coherences reflecting both intra- and intermolecular types of relaxation processes [47].

C. Calculations

Equation (7) gives the signal intensity for the Ξ-excitation scheme as the modulus squared of the sum of oscillating, $e\neq e'$, and nonoscillating, $e=e$, terms, with oscillating frequencies that are proportional to the energy difference between pairs of hyperfine levels in the intermediate $|E\rangle$ state. Similarly, Eq. (9) describes the signal intensity for the *V*-excitation scheme, in this case, in terms of oscillating, $i\neq i'$, and nonoscillating, $i=i'$ terms with frequencies proportional to the energy difference between pairs of hyperfine levels in the initial state $|I\rangle$. In each scheme, the electronic angular momentum of the three matter states accessed by a given set of grating and probe transitions and the polarization vectors of each laser beam are used to compute geometrical factors to be summed over the unresolved hyperfine levels. The elements of that summation can be organized into a matrix of geometric factors $a_{ee'}$ ($a_{ii'}$) indexed by the pairs of hyperfine levels. The diagonal elements in this matrix correspond to terms where $e=e$ ($i=i$), which makes their associated complex frequencies $\Omega_{ee'}=i\Gamma_{ee'}$ ($\Omega_{ii'}=i\Gamma_{ii'}$). By assuming that the decay rates are equal for each of the hyperfine states, these zero-frequency terms can be summed into a single constant term A_0. The off-diagonal matrix elements correspond to the amplitudes of $e\neq e'$ ($i\neq i'$) hyperfine pairs that give rise to oscillatory terms in the intensity expressions in Eqs. (7) and (9).

To illustrate how the oscillating and nonoscillating contributions to the signal can be obtained from fits of the model to the experimental data, we consider the Ξ-excitation scheme used to probe the $A\,^2\Sigma^+$ state hyperfine structure. Since the amplitudes corresponding to $\Omega_{ee'}$ and $\Omega_{e'e}$ are equal in magnitude, summing the two terms gives

$$\begin{aligned} &a_{e'e}\exp(i\Omega_{e'e}\tau)+a_{ee'}\exp(i\Omega_{ee'}\tau)\\ &\quad=a_{ee'}[\exp(i\Omega_{e'e}\tau)+\exp(i\Omega_{ee'}\tau)]\\ &\quad=a_{ee'}\exp(-\Gamma_{ee'})[\exp(i\omega_{e'e}\tau)+\exp(i\omega_{ee'}\tau)]\\ &\quad=2a_{ee'}\exp(-\Gamma_{ee'})\cos(\omega_{ee'}\tau), \end{aligned} \tag{11}$$

where $\Gamma_{ee'}=\Gamma_{e'e}$ has been assumed. The expression for the observed TC-RFWM intensity as a function of time for the three unresolved hyperfine levels of the $A\,^2\Sigma^+$ state, which gives rise to three beat frequencies, is then given by

$$\begin{aligned} I\propto[&A_0e^{-\Gamma t}+A_{12}\cos(\omega_{12}t)e^{-\Gamma_{12}t}+A_{23}\cos(\omega_{23}t)e^{-\Gamma_{23}t}\\ &+A_{13}\cos(\omega_{13}t)e^{-\Gamma_{13}t}]^2. \end{aligned} \tag{12}$$

In what follows, we refer to A_0 as the nonoscillating amplitude and the $A_{ij}=2a_{ij}$ as the oscillating amplitudes. These coefficients can be calculated directly from the expressions given in Eqs. (7) and (9) by performing the sums over the hyperfine states involved for a set of grating and probe transitions, and a specific laser polarization configuration.

D. Model predictions

One of the main advantages of using the TC-RFWM technique to do quantum beat spectroscopy is the state selectivity inherent to this two-color nonlinear technique. The signal intensity expressions from Eqs. (7) and (9) in each case predict that only one of the three states involved in the mixing process will contribute to the generation of quantum beats as a function of the time delay τ between the grating and probe-laser pulses. For the Ξ- and V-excitation schemes, the beats are predicted to result from the unresolved hyperfine structure of the $A\,^2\Sigma$, $v=0$ and $X\,^2\Pi_{1/2}$, $v=0$ states, respectively. The physical explanation for this state selectivity is that, by varying the the delay time τ, the probe pulse directly interrogates the dynamics of the laser-induced grating during its field-free evolution. As expressed by Eq. (12), the time-resolved signal is a square of the sum of a constant term and three oscillating terms. Thus, the relative size and sign of the amplitudes of these terms play a crucial role in determining the detail shape of the interferences in the time-decay curves.

The population and polarization grating configurations shown in Fig. 1 have been investigated. Recall that population gratings are created with grating beams of parallel polarizations and consist of a pattern of spatially varying light intensity. Polarization gratings are generated at the overlap of cross-polarized beams, so they contain no intensity variation across the grating fringes, only a variation in light polarization [6,46]. Some work has suggested that there should be no observable oscillating component in the time-resolved TC-RFWM signal from population gratings in the weak-field regime [11]. Quantum beats however, were observed in a population grating configuration [29] and therefore, we are particularly interested in looking at this configuration in more detail. Several key model predictions are shown in Fig. 4, which displays the calculated dependence of the individual signal amplitudes on the relative linear polarization states of the grating, probe and signal beams. These calculations are for the $R(0.5)$ grating transition and the $P(1.5)$ probe transition in the Ξ-excitation scheme shown in Fig. 2(b).

In the case of population gratings with parallel grating beam polarizations, $\varepsilon_{g1}\|\varepsilon_{g2}$, the nonoscillating amplitude is much larger than the oscillating amplitudes for almost all orientations of the signal beam polarization relative to the probe beam polarization. As the angle between the probe and the signal beam polarizations, θ_{p-s}, is increased to 90°, however, the nonoscillating amplitude approaches zero as shown in Fig. 4(a). Since the oscillating amplitudes remain nonzero at $\theta_{p-s}\simeq 90°$, the oscillating terms become a significant fraction of the total signal for this polarization configuration. This trend is followed for all probe polarization orientations and thus, the model predicts that $\theta_{p-s}\simeq 90°$ optimizes the relative size of beats in the signal, while at the same time, minimizing the overall magnitude of the signal. Further, Fig. 4(b) shows that, for the maximum-beat configuration with $\theta_{p-s}\simeq 90°$, the largest total signal should be observed when the probe polarization is at 45° with respect to the grating polarization vectors.

The model predicts a different trend for the case of polarization gratings where the grating beam polarizations are orthogonal to one another, $\varepsilon_{g1}\perp\varepsilon_{g2}$. While the visibility of beats in the population grating case ($\varepsilon_{g1}\|\varepsilon_{g2}$) is predicted to be strongly dependent on the signal beam polarization orientation, ε_s, the relative beat size with the polarization grating configuration remains relatively independent of ε_s. This model prediction is illustrated in Fig. 4(c).

IV. EXPERIMENT

A schematic of the experimental arrangement is shown in Fig. 5. Two Nd:yattrium-aluminum garnet (YAG)-pumped dye lasers were used to acquire time-resolved TC-RFWM signal intensities from selected electronic transitions in NO. For the Ξ-excitation scheme shown in Fig. 2(b) tunable ultraviolet (UV) light at 226 nm, generated by frequency doubling the output of one dye laser, was used to excite $A\,^2\Sigma^+$, $v=0\leftarrow X\,^2\Pi_{1/2}$, $v=0$ rotational transitions. The direct output of the second dye laser at 600 nm was used to subsequently probe $E\,^2\Sigma^+$, $v=0\leftarrow A\,^2\Sigma^+$, $v=0$ rotational transitions. For the V-excitation scheme shown in Fig. 2(a), the output of the second dye laser was frequency doubled to produce light at 215 nm to excite $A\,^2\Sigma^+$, $v=1\leftarrow X\,^2\Pi_{1/2}$, $v=0$ rotational transitions. The output pulses from both lasers were linearly polarized, with a duration of ~8 ns and a frequency bandwidth of ~1.5 GHz. The intensity of light was typically between 50 and 150 μJ for the 226-nm and 215-nm beams and 10–20 μJ for the 600-nm beam. All laser beams were unfocused and had a diameter of ~2 mm.

A pulsed valve was used to produce a pure beam of NO molecules. The backing pressure of the valve was ~1.4 atm,

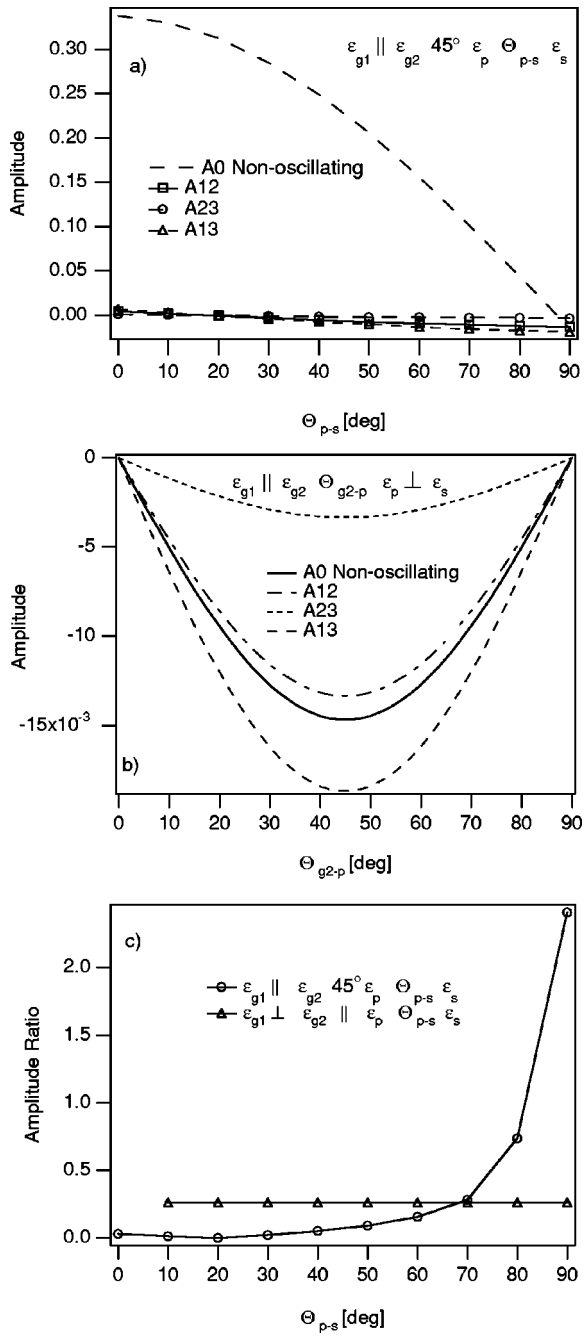

FIG. 4. (a) Calculated amplitudes as a function of the relative probe and signal polarization angle. (b) Calculated amplitudes as a function of the relative grating and probe polarization angle. (c) Ratio of the sum of the oscillating amplitudes to the nonoscillating amplitude for the population and polarization grating configurations.

while the background pressure in the chamber was $\sim 1 \times 10^{-5}$ Torr. Adiabatic cooling in the supersonic expansion resulted in a molecular beam characterized by low translational and rotational temperatures. This cooling caused a significant reduction of the components of the molecular velocity perpendicular to the grating fringes, thereby diminishing the rate of grating decay due to residual thermal motion of the NO.

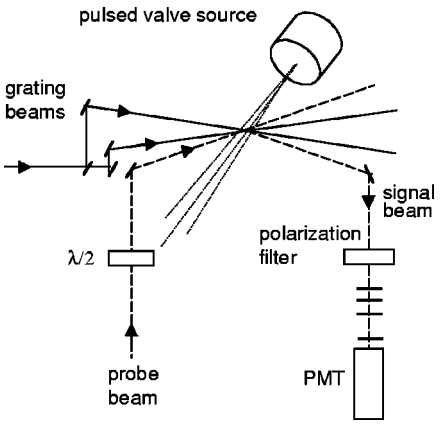

FIG. 5. Experimental arrangement used for TC-RFWM.

In all of our TC-RFWM experiments we used the same forward-box phase-matching geometry, in which the three incoming laser beams are nearly copropagating and generate gratings with relatively large fringe spacings. While this geometry does not produce Doppler-free measurements, it results in relatively large grating fringe spacings, which reduce the grating decay due to molecular motion and increase the phase-matching wavelength range [39]. A beamsplitter was used to divide the grating beam into two beams that were crossed at a small angle ($\sim 2°$) in the NO molecular beam. The probe beam was then crossed with the grating beams at an angle that satisfied the phase-matching constraint equivalent to the Bragg scattering condition shown in Fig. 1 [19]. Our arrangement resulted in a typical fringe spacing of ~ 13 microns and ~ 150 fringes in the interaction region where the laser beams overlapped the molecular beam.

A Fresnel rhomb half-waveplate was used to rotate the polarization of either one of the grating beams or the probe beam. A Glan-Taylor polarizer in the signal beam path provided a means for detecting a single linearly polarized component of the signal beam. Prior to detection with a photomultiplier tube, the signal beam was spatially filtered with a pair of lenses and a pinhole. To further improve our signal-to-noise ratio, which was limited by background scattered light, wavelength filters were used.

A gated boxcar integrator was used to average the signal over a fixed number of laser shots. A digital delay generator was used to control the time delay between the grating forming laser pulses and the probe-laser pulse. Experimental grating decay curves were obtained by fixing the laser beam frequencies on resonance with a set of rotational transitions and varying the time delay between the arrival of the grating and probe-laser pulses for various beam polarization configurations, thereby providing a time-resolved probe of the hyperfine coherences prepared by the grating beams.

V. RESULTS AND DISCUSSION

Measurements of TC-RFWM signal decay curves were made for various rotational transitions and polarizations configurations by using the Ξ- and V-excitation schemes shown in Fig. 2. Figure 6 shows a series of decay curves obtained by using the polarization configuration and the V-excitation

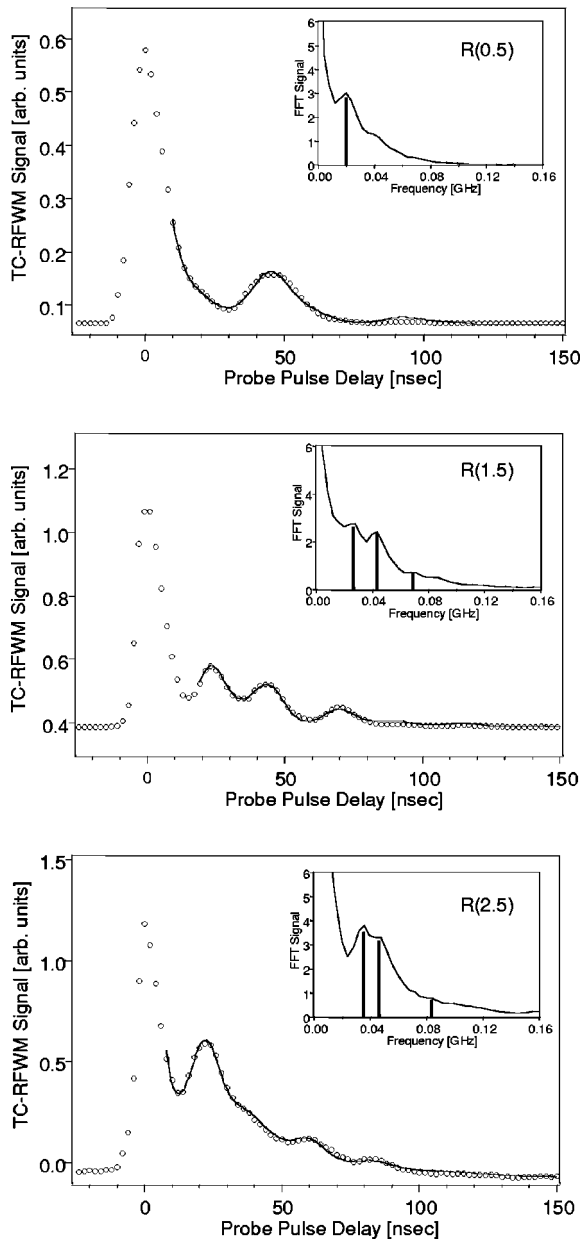

FIG. 6. Measured decay curves obtained by using the *V*-excitation scheme in Fig. 2(a) and the polarization grating configuration showing quantum beats due to the hyperfine structure of several J levels of the $X\,^2\Pi_{1/2}$, $v=0$ state of NO. Open circles are the experimental data. The solid lines are fits of Eq. (13) to the data. Inserts: FFT of the time-domain data.

scheme. Quantum beats reflecting the hyperfine structure of the $J=0.5$, 1.5, and 2.5 levels of $X\,^2\Pi_{1/2}$, $v=0$ ground state are clearly visible. To analyze our results we used time-domain fits to the data to obtain a set of beat frequencies and their associated amplitudes for each time-decay curve. The functional form of the fit is derived from the final form of the signal intensity expression given by Eq. (12):

$$I(t)=c+e^{-2t\Gamma}[A_0+A_{12}\cos(\omega_{12}t)+A_{23}\cos(\omega_{23}t)+A_{13}\cos(\omega_{13}t)]^2. \quad (13)$$

TABLE I. Hyperfine energy-level beat frequencies in MHz as a function of v and J in the $A\,^2\Sigma^+$ state of NO.

	$(F=J-1)-(F=J)$			$(F=J)-(F=J+1)$		
$J=N+1/2$	Observed	Calculated		Observed	Calculated	
	$v=0$	$v=1$	$v=3$	$v=0$	$v=1$	$v=3$
1.5	15.3±0.6	10.4	13.5	45±1	44.6	42.1
2.5	16.1±0.6	12.7	15.9	35±1	37.7	34.7
3.5	16.9±0.6	13.6	16.8	33±1	34.3	31.2
4.5	17.8±0.7	14.1	17.2	33±1	32.5	29.2

Here, A_{ij} and ω_{ij} are identical to the amplitudes and frequencies given in Eq. (12). This expression is appropriate for both the Ξ- and *V*-excitation schemes. The earliest part of the time-decay curves is excluded from the fitting range because only those terms for delay times greater than zero are included in the model. We have assumed that the decay rates are independent of the specific hyperfine level accessed so that $\Gamma=\Gamma_{12}=\Gamma_{13}=\Gamma_{23}$. The decay rate Γ, therefore represents the average overall decay due to the lifetime of the $A\,^2\Sigma^+$ state and residual transverse motion in the molecular beam.

An alternative method of obtaining the beat frequencies and amplitudes is to perform fast fourier transforms (FFT) on the data. Examples are shown as inserts in Fig. 6. While FFT spectra offer the same type of information as the fits of time-domain data, they were less valuable in making direct comparisons between the theoretical predictions and our experimental data due to their limited frequency resolution. The time-domain fits yielded significantly better statistical uncertainties for the beat frequencies and relative amplitudes.

A. Frequencies

The range of energy splittings and the corresponding beat frequencies that could be observed was limited by several factors including laser bandwidth, finite duration of the laser pulses, and the grating lifetime. The upper frequency limit is dictated by the duration of the laser pulses of ~8 ns, which translates into ~125 MHz. The lower end of the frequency limit is determined by the lifetime of the gratings, ~150 ns. This results in the lower-frequency resolution limit of ~7 MHz. Tables I and II give the results of our analysis of decay curves obtained by using the Ξ- and *V*-excitation schemes to probe the hyperfine structure of the $A\,^2\Sigma^+$, $v=0$ excited state and the $X\,^2\Pi_{1/2}$, $v=0$ ground state, respectively. The uncertainties listed are the standard deviations computed

TABLE II. Hyperfine energy-level beat frequencies in MHz as a function of J in the $X\,^2\Pi_{1/2}$, $v=0$ state of NO.

	$(F=J-1)-(F=J)$		$(F=J)-(F=J+1)$	
$J=N-1/2$	Observed	Ref. [40]	Observed	Ref. [40]
0.5			19.8±0.2	21±1.5
1.5	26.1±0.2	27±1.5	42.9±0.2	42±1.5
2.5	34.7±0.3	36±1.5	47.6±0.3	45±1.5

from analysis of multiple decay curves. The statistical errors from the fits were about five times smaller than the standard deviations.

In Table I we see significant variations between the observed $v=0$ and the calculated $v=1$ and $v=3$ frequencies for all J states. The differences in the reported hyperfine coupling parameters for the $v=1$ and $v=3$ levels of the $A\,^2\Sigma^+$ state [42,41] suggest that the variation in the hyperfine coupling strengths across different vibrational levels is large enough to account for the disagreement of our observations for $v=0$ splittings when compared with results of the $v=1$ and $v=3$ calculations. The magnitude of the $v=0$ frequencies and their trend with increasing J, however, does confirm that the beat frequencies in this TC-RFWM excitation scheme originate from the hyperfine structure of the intermediate $A\,^2\Sigma^+$ state.

The beat frequencies obtained for the $X\,^2\Pi_{1/2}$, $v=0$ ground state are shown in Table II. Previously measured values [40] are also given for comparison. The level of agreement between the observed beats and the previously measured hyperfine structure in the ground state is excellent. The agreement with increasing J is also evident. Note that we see no beats due to the $A\,^2\Sigma^+$ state in the decay curves obtained with the V-excitation scheme thereby demonstrating the truly state-selective nature of this technique to probe quantum interferences.

B. Amplitudes

The model for the TC-RFWM signal calculates the contribution of individual oscillating and nonoscillating amplitudes for a particular polarization configuration and set of rotational transitions. In the course of our analysis it became clear that the calculated amplitudes and the data amplitudes did not agree. We believe this is due to the finite duration of our laser pulses. To investigate this effect on the amplitudes, we performed convolutions of the calculated grating decay curves with an 8-ns Gaussian envelope to simulate the effect of a finite probe pulse width in time. Convoluted theoretical grating decay curves were generated by combining the experimentally determined beat frequencies and decay factors with the calculated oscillating and nonoscillating term amplitudes. Performing the same fitting routine on these theoretical curves before and after the convolution showed that the convolution process does indeed introduce a significant change in the relative magnitudes of the individual fit amplitudes. In Fig. 7 the solid line shows a calculated convoluted curve, which agrees fairly well with the experimental curve. The dashed line shows a fit of Eq. (12) to the data. In general, the differences observed in the individual amplitudes are less than 20% when comparing the calculated convoluted curves and the fit curves. In what follows, calculated amplitudes refer to amplitudes determined by using the convoluted calculated curves.

C. Polarization effects

We explored many different polarization configurations and the general trends observed in the experimental data match very well the predictions of the model. For the population grating configuration, the component of the signal parallel to the polarization of the probe beam shows no perceptible oscillating structure. This seems to confirm the suggestion that population gratings should exhibit no beats [11]. As can be seen in Fig. 8, however, the component of the signal rotated perpendicular to the probe shows pronounced oscillations corresponding to beats between the $J=2.5$ hyperfine levels of the $A\,^2\Sigma^+$, $v=0$ state. This observation confirms the predictions illustrated in Fig. 4(a).

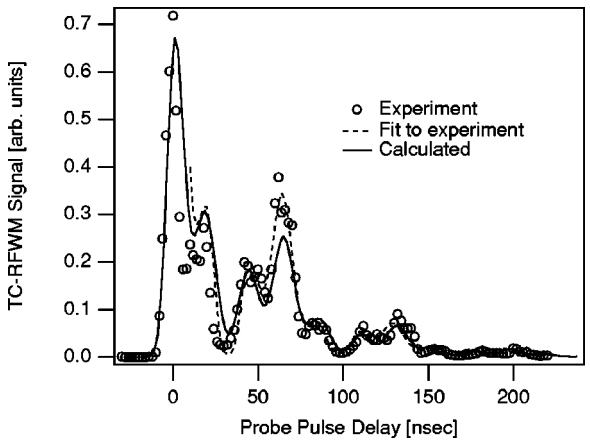

FIG. 7. Measured and calculated decay curves obtained by using the Ξ-excitation scheme shown in Fig. 2(b) and the population grating configuration. The grating beams were tuned to the $R(0.5)$ transition and the probe was tuned to the $R(1.5)$ transition.

We can also compare the population grating result in Fig. 8 to the polarization grating case in Fig. 9. It shows the time evolution of the polarization grating signal as a function of the probe-signal polarization angle. During the experiment, the signal intensity decreased with the decrease in the probe-signal polarization angle. Thus we show the TC-RFWM decay signals each scaled individually, to make a direct comparison between their shapes possible. We see that the general shape of the signal remains the same for all probe-

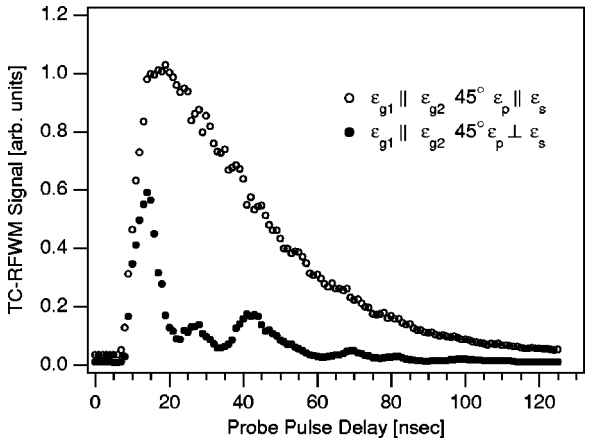

FIG. 8. Measured decay curves for two orientations of the signal beam polarization in the population grating configuration obtained by using the Ξ-excitation scheme shown in Fig. 2(b). The grating beams were tuned to the $R(1.5)$ transition and the probe beam was tuned to the $P(2.5)$ transition.

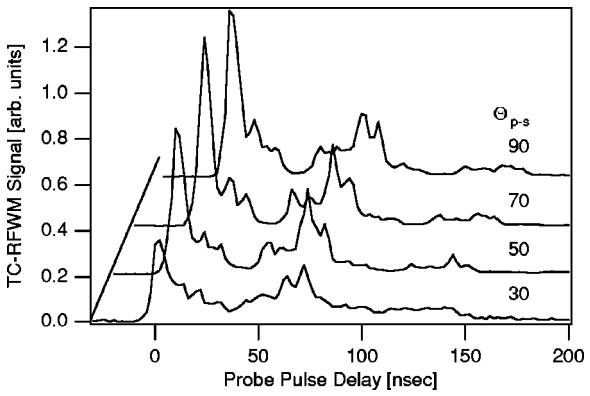

FIG. 9. Measured decay curves for several different values of the angle between the probe and signal beam polarization orientations in the polarization grating configuration obtained by using the Ξ-excitation scheme shown in Fig. 2(b). To aid the comparison of their shapes, each curve has been scaled separately in intensity to agree at zero delay. The grating beams were tuned to the $R(0.5)$ transition and the probe was tuned to the $R(1.5)$ transition.

signal polarization angles. This agrees well with the predictions of the model shown in Fig. 4(c) illustrating that the amplitudes of the different oscillating terms remain in the same proportion while their absolute size decreases with the decreasing probe-signal polarization angle.

Figure 10 shows a comparison of the experimental and theoretical ratios of the nonoscillating amplitudes to the sum of the oscillating amplitudes as a function of the angle between the probe and signal beam polarization vectors for the $\varepsilon_{g1} \| \varepsilon_{g2} 45° \varepsilon_p$ population grating configuration. The error bars reflect the standard deviation of several data sets. The experimental data show good qualitative agreement with the model predictions, although both horizontal and vertical offsets are evident. The horizontal offset suggests a systematic error of approximately $-5°$ in the probe-signal polarization

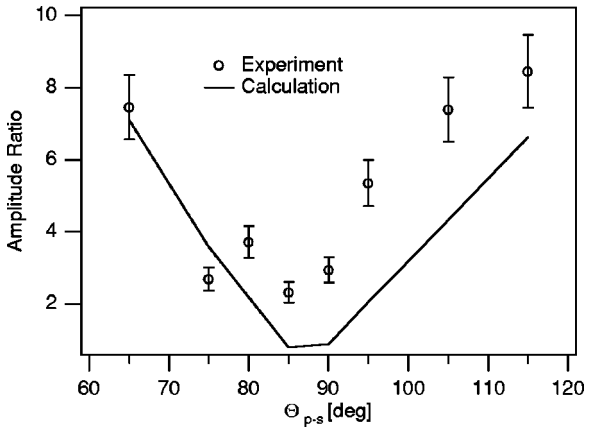

FIG. 10. Measured and calculated ratio of the nonoscillating amplitude to the sum of the oscillating amplitudes as a function of the angle between the probe and signal beam polarization orientations in the population grating configuration obtained by using the Ξ-excitation scheme shown in Fig. 2(b). The grating beams were tuned to the $R(0.5)$ transition and the probe was tuned to the $R(1.5)$ transition.

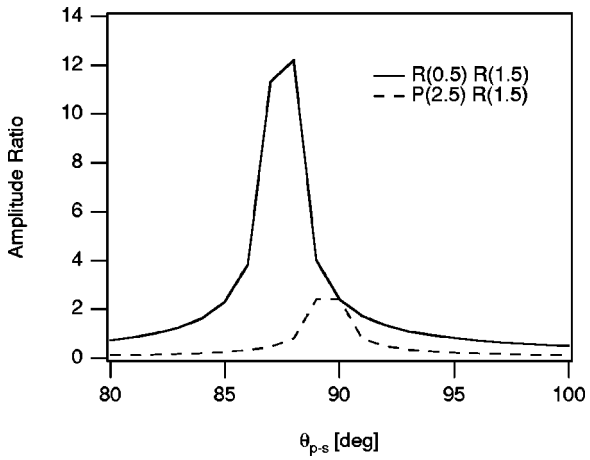

FIG. 11. Calculated ratio of the sum of oscillating amplitudes to the nonoscillating amplitudes as a function of the angle between the probe and signal beam polarization orientations in the population grating configuration obtained by using the Ξ-excitation scheme shown in Fig. 2(b). For the same $R(1.5)$ probe transition, results are compared for two different grating transitions: the $R(0.5)$ and $P(2.5)$, which access the same $J=1.5$ level of the $A\,^2\Sigma^+$, $v=0$ state.

angles. The half-waveplate in our setup rotates the probe polarization by the angle 2α, where α is the angle between the original probe beam and the waveplate polarization axis. Therefore, even a seemingly small error of 2.5° degrees becomes significant after being augmented by the factor of 2. The vertical offset between the experimental and predicted values implies that the observed nonoscillating component of the signal is consistently greater than that predicted by the model. This could also be accounted for by an uncertainty in the polarization integrity of the probe beam. Since the nonoscillating term dominates the signal for all probe-signal polarization angles, except around $\varepsilon_p \perp \varepsilon_s$, even a 5% polarization impurity of the probe beam would make a significant nonoscillating contribution to the signal.

Finally, in addition to polarization effects, the model also predicts the change in relative signal amplitudes introduced by varying the transitions used to excite a particular intermediate state. An example is shown in Fig. 11 for the population grating polarization configuration. The graph shows the ratio of the sum of oscillating amplitudes to the nonoscillating amplitude for the $J=1.5$ level of the $A\,^2\Sigma^+ v=0$ state excited by two different grating transitions. The differences in the peak heights suggest that the signal obtained with the $R(0.5)$ grating transition should show more pronounced oscillations than the signal obtained by using the $P(2.5)$ grating transition. Figure 12 shows the corresponding measured decay curves. Both figures suggest that the relative size of the oscillating terms in the case of the $R(0.5)$ grating transition is much larger than in the $P(2.5)$ case. The theoretical graph in Fig. 11 shows this directly with the size of the amplitude ratio peaks, whereas the experimental curves in Fig. 12 illustrate it with the relative depth of the signal modulation. This is another case where there is a strong agreement between the calculations and the experiment, demonstrating the overall effectiveness of the model.

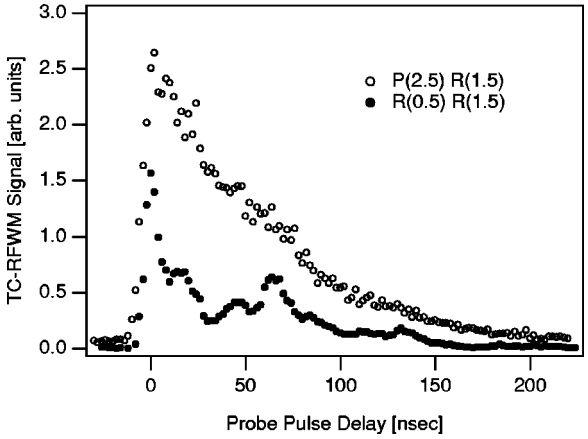

FIG. 12. Measured decay curves using the population grating configuration and the Ξ-excitation scheme shown in Fig. 2(b). Results using the $R(0.5)$ and $P(2.5)$ grating transitions are compared. The same $R(1.5)$ probe transition was used in each case.

VI. CONCLUSIONS

Experiments have been performed on NO to explore laser polarization effects in time-resolved TC-RFWM measurements. The results have been used to test a model that describes the application of this technique for doing high-resolution quantum beat spectroscopy. The agreement of various model predictions with the experimental observations demonstrates that TC-RFWM can be successfully applied to state-selective studies of energy structures that are orders of magnitude smaller than the laser bandwidth. By analyzing the frequency structure of the time-decay curves, we obtained precise measurements of the hyperfine structure splitting of several rotational levels of the $X\,^2\Pi_{1/2}$, $v=0$ ground state and $A\,^2\Sigma^+$, $v=0$ excited state of NO. Moreover, the hyperfine structure of only one of the three electronic states involved in each excitation scheme was observed to contribute to the beats in the signal, thereby demonstrating the valuable state-selective character of the TC-RFWM technique.

There are many directions for future experimental work in this area. A comparison of calculated and observed amplitudes of the oscillating and nonoscillating terms in the time-resolved TC-RFWM signal indicate that a treatment of the finite width of the laser pulses would be useful for quantitative analysis. Also exciting is the promise of applying the results demonstrated here to investigations with ultrashort laser pulses to use the advantages of TC-RFWM in studies of other types of coherent excitations, for example, rotational and vibrational wave packets.

ACKNOWLEDGMENTS

E. Sarajlic gratefully acknowledges support from Bryn Mawr College. This work was funded by the National Science Foundation, Grant No. PHY-9623569.

[1] R. W. Boyd, *Nonlinear Optics* (Academic Press, Boston, 1992); Y. R. Shen, *The Principles of Nonlinear Optics* (Wiley, New York, 1984), H. J. Eichler, P. Günter, and D. W. Pohl, *Laser-Induced Dynamic Gratings* (Springer-Verlag, Berlin, 1986).
[2] R. L. Farrow and D. J. Rakestraw, Science **257**, 1894 (1992).
[3] D. S. Green, T. G. Owano, S. Williams, D. G. Goodwin, R. N. Zare, and C. H. Kruger, Science **259**, 1726 (1993).
[4] J. T. Fourkas and M. D. Fayer, Acc. Chem. Res. **25**, 227 (1992).
[5] P. H. Vaccaro in *Molecular Dynamics and Spectroscopy by Stimulated Emission Pumping*, edited by H. L. Dai and R. W. Field, Advances in Physical Chemistry Series, edited by C.-Y. Ng (World Scientific, Singapore, 1995), Vol. 4, p. 1.
[6] J. T. Fourkas, R. Trebino, and M. D. Fayer, J. Chem. Phys. **97**, 69 (1992); **97**, 78 (1992).
[7] G. Hall and J. Whittaker, J. Chem. Soc., Faraday Trans. **90**, 1 (1994).
[8] See for example, *Ultrashort Laser Pulses*, edited by W. Kaiser (Springer-Verlag, Berlin, 1993); G. R. Fleming, *Chemical Applications of Ultrafast Spectroscopy* (Oxford University Press, New York, 1986).
[9] S. Mukamel, *Principles of Nonlinear Optical Spectroscopy* (Oxford University Press, New York, 1995).
[10] M. Schmitt, G. Knopp, A. Materny, and W. Kiefer, J. Phys. Chem. **102**, 4059 (1998).
[11] Y. Tang, J. P. Schmidt, S. A. Reid, J. Chem. Phys. **110**, 5734 (1999).
[12] T. S. Yang, R. Zhang, A. B. Myers, J. Chem. Phys. **100**, 8573 (1994).
[13] M. Schmitt, G. Knopp, A. Materny, and W. Kiefer, Chem. Phys. Lett. **280**, 339 (1997).
[14] A. A. Survenev, R. Tadday, and T. Dreier, Phys. Rev. A **58**, 4102 (1998).
[15] M. Motzkus, S. Pedersen, and A. H. Zewail, J. Phys. Chem. **100**, 5620 (1996).
[16] T. R. Brewer, J. T. Fourkas, and M. D. Fayer, Chem. Phys. Lett. **203**, 344 (1992).
[17] T. Dreier and D. J. Rakestraw, Appl. Phys. B: Photophys. Laser Chem. **50**, 479 (1990).
[18] A. A. Suvernev, A. Dreizler, T. Dreier, and J. Wolfrum, Appl. Phys. B: Photophys. Laser Chem. **61**, 421 (1986).
[19] T. J. Butenhoff and E. A. Rohlfing, J. Chem. Phys. **98**, 5460 (1993); **98**, 5469 (1993).
[20] S. Williams, J. D. Tobiason, J. R. Dunlop, and E. A. Rohlfing, J. Chem. Phys. **102**, 8342 (1995).
[21] P. P. Radi, H.-M. Frey, B. Mischler, A. P. Tzannis, P. Beaud, and T. Gerber, Chem. Phys. Lett. **265**, 271 (1997).
[22] E. F. McCormack, F. Di Teodoro, J. M. Grochocinski, and S. T. Pratt, J. Chem. Phys. **109**, 63 (1998).
[23] A. Kumar, C.-C. Hsiao, W.-C. Hung, and Y.-P. Lee, J. Chem. Phys. **109**, 3824 (1998).
[24] A. Kumar, C.-C. Hsiao, Y.-Y. Lee, and Y.-P. Lee, Chem. Phys. Lett. **297**, 300 (1998).
[25] M. N. R. Ashfold, D. W. Chandler, C. C. Hayden, R. I.

McKay, and A. J. R. Heck, Chem. Phys. **201**, 237 (1995).
[26] E. F. McCormack, P. M. Dehmer, J. L. Dehmer, and S. T. Pratt, J. Chem. Phys. **102**, 4740 (1995).
[27] F. Di Teodoro and E. F. McCormack, J. Phys. B **32**, 4389 (1999).
[28] H. Bitto and J. R. Huber, Opt. Commun. **80**, 184 (1990); Acc. Chem. Res. **25**, 65 (1992).
[29] E. F. McCormack, S. T. Pratt, P. M. Dehmer, and J. L. Dehmer, Chem. Phys. Lett. **227**, 656 (1994).
[30] A. Sieradzan, P. Kulatunga, and M. Havey, Phys. Rev. A **52**, 4447 (1995).
[31] I. M. Povey, R. T. Carter, H. Bitto, and J. R. Huber, Chem. Phys. Lett. **248**, 470 (1996).
[32] J. A. Gray, R. L. Farrow, J. L. Durant, and L. R. Thorne, J. Chem. Phys. **99**, 4327 (1993) and references therein.
[33] R. Tadday, A. A. Survenev, T. Dreier, and J. Wolfrum, Chem. Phys. Lett. **268**, 117 (1997).
[34] A. H. Zewail, *Femtochemistry: Ultrafast Dynamics of the Chemical Bond* (World Scientific, Singapore, 1994).
[35] T. S. Rose, W. L. Wilson, G. Wackerle, and M. D. Fayer, J. Chem. Phys. **86**, 5370 (1987); J. Phys. Chem. **91**, 1704 (1987).
[36] T. A. W. Wasserman, P. H. Vaccaro, and B. R. Johnson, J. Chem. Phys. **106**, 6314 (1997); **108**, 7713 (1998).
[37] F. Di Teodoro and E. F. McCormack, Phys. Rev. A **57**, 162 (1998).
[38] S. Williams, E. A. Rohlfing, L. A. Rahn, and R. N. Zare, J. Chem. Phys. **106**, 3090 (1997).
[39] S. Williams, R. N. Zare, and L. A. Rahn, J. Chem. Phys. **101**, 1072 (1994).
[40] P. Kirstiansen, J. Mol. Spectrosc. **66**, 177 (1977).
[41] T. Bergeman and R. N. Zare, J. Chem. Phys. **61**, 4500 (1974).
[42] R. J. Miller, W. L. Glab, and B. A. Bushaw, J. Chem. Phys. **91**, 3277 (1989).
[43] J. G. Fujimoto and T. K. Yee, IEEE J. Quantum Electron. **QE-22**, 1215 (1986); Y. Prior, *ibid.* **QE-20**, 37 (1984), and references therein.
[44] R. N. Zare, *Angular Momentum: Understanding Spatial Aspects in Chemistry and Physics* (Wiley, New York, 1988).
[45] Note that this geometric factor differs by a factor of $(-1)^{J_U+J_E}(2F_i+1)(2F_u+1)$ from the geometric factor presented in Eq. (22) of Ref. [27]. The expression given here allows a direct comparison of the factors for the case of $\mathcal{I}=0$ with the geometrical factors of Ref. [38].
[46] J. T. Fourkas, T. R. Brewer, H. Kim, and M. D. Fayer, Opt. Lett. **16**, 177 (1990); J. Chem. Phys. **95**, 5775 (1991).
[47] S. Williams, L. A. Rahn, and R. N. Zare, J. Chem. Phys. **104**, 3947 (1996).
[48] S. S. Vianna, P. Nussenzveig, W. C. Magno, and J. W. R. Tabosa, Phys. Rev. A **58**, 3000 (1998).
[49] H. Li and W. Kong, J. Chem. Phys. **107**, 3774 (1997); **109**, 4782 (1998).
[50] T. Müller, T. A. Wasserman, and P. H. Vaccaro, J. Chem. Phys. **108**, 4 (1998).